

Control and Pointing Challenges of Antennas and (Radio) Telescopes

W. Gawronski¹

Extremely large telescopes will be constructed in the near future, and new radio telescopes will operate at significantly higher radio frequencies; both features create significantly increased pointing-accuracy requirements that have to be addressed by control system engineers. This article presents control and pointing problems encountered during design, testing, and operation of antennas, radio telescopes, and optical telescopes. This collection of challenges provides information on their current status, helps to evaluate their importance, and is a basis for discussion on ways to improve antenna pointing accuracy.

I. Introduction

In this article, we present pointing and control challenges that new antennas, radio telescopes, and optical telescopes will meet. Radio telescopes perform operations at radio frequencies lower than optical telescopes. They use parabolic dishes rather than mirrors. The dish size is larger (up to 100 m) than mirrors of optical telescopes (up to 10 m). Antennas are radio telescopes that not only can receive radio frequency signals but also can send them. They are used for spacecraft communication. The newly designed antennas, radio telescopes, and telescopes have to satisfy control and pointing requirements that challenge existing technology. In order to increase the data rate, the antennas are required to communicate at higher radio frequencies: from S-band (2.3 GHz), to X-band, (8.5 GHz), to Ka-band (32 GHz). The increased frequency requires more precise pointing: 28 mdeg for S-band, 8 mdeg for X-band, and 2 mdeg for Ka-band. The telescope size also increases, from the 12-m Keck Telescope to the 30- or 50-m future telescopes now on drawing boards. The increased size creates multiple pointing and control challenges.

II. Antenna and Telescope Examples

A. NASA Deep Space Network

The NASA Deep Space Network (DSN) antennas communicate with spacecraft by sending commands (uplink) and by receiving information from spacecraft (downlink). To assure continuous tracking during Earth rotation, the antennas are located at three sites: Goldstone (California), Madrid (Spain), and Canberra (Australia). The signal frequencies are 8.5 GHz (X-band) and 32 GHz (Ka-band). The dish size of the antennas is either 34 m or 70 m. An example of a 70-m antenna is shown in Fig. 1. The

¹ Communications Ground Systems Section.

The research described in this publication was carried out by the Jet Propulsion Laboratory, California Institute of Technology, under a contract with the National Aeronautics and Space Administration.

antenna dish rotates with respect to the horizontal (or elevation) axis. The whole antenna structure rotates on a circular track (the azimuth track) with respect to the vertical (or azimuth) axis. For the Ka-band frequency, the required tracking accuracy is on the order of 1 mdeg. This requirement is a driver for the control system upgrade of the antennas. In [1,2], one can find descriptions of the DSN antenna control systems. Articles reporting on DSN antenna research, including control systems, can be found at this publication's Web site [58] and the Deep Space Network web site [59].

B. The Large Millimeter Telescope

The Large Millimeter Telescope (LMT) project is the joint effort of the University of Massachusetts at Amherst and the Instituto Nacional de Astrofísica, Óptica, y Electrónica (INAOE) in Mexico. The LMT is a 50-m-diameter radio telescope designed for principal operation at wavelengths between 1 mm and 4 mm. The telescope is being built atop Sierra Negra (4640 m), a volcanic peak in the state of Puebla, Mexico. The telescope construction is expected to be completed in 2005. The LMT will be a significant step forward in antenna design. In order to reach its pointing accuracy specifications, it must outperform every other telescope in its frequency range. The antenna designer expects that the telescope will point to its specified accuracy of 1 arcsec under conditions of low winds and stable temperatures. For more about the LMT, see [60].

C. APEX Telescope

The Max Planck Institute for Radioastronomy awarded a contract to Vertex Antennentechnik (Germany) to install the 12-m APEX (Atacama Pathfinder Experiment) telescope in the Chilean Atacama desert at Llano de Chajnantor at 5000-m altitude. This telescope will be used for observations in the submillimeter wavelength range. The overall surface accuracy of 20 μm and the pointing accuracy of 0.6 arcsec have been proven during acceptance testing, which was carried out in 2004.



Fig. 1. NASA/JPL 70-m antenna at Goldstone, California.

D. ESA Deep Space Antennas

For use in deep space, high elliptical orbit missions, and future missions to Mars, the European Space Agency (ESA) procured 35-m deep-space ground stations. The antennas are designed for frequencies up to 35 GHz and a pointing accuracy of 6 mdeg. The first antenna has been installed in Australia and has proven its compliance to the specifications. The second antenna is under construction in Spain. The 35-m antenna incorporates a full-motion pedestal with a beam-waveguide system.

E. ALMA Prototype

The Atacama Large Millimeter Array (ALMA) has been successfully installed and tested by Vertex; a brief description can be found at [61]. The pointing accuracy of the 12-m ALMA telescope is 0.6 arcsec. The control system must handle very accurate movement at sidereal tracking velocities as well as several extremely fast switching functions. To do this, the drives are designed to accelerate up to 24 deg/s^2 , which is very unusual for a telescope of this size.

F. The Thirty Meter Telescope

The Thirty Meter Telescope (TMT) will be the first of the giant optical/infrared ground-based telescopes addressing these compelling areas in astrophysics: the nature of dark matter and dark energy, the assembly of galaxies, the growth of structure in the universe, the physical processes involved in star and planet formation, and the characterization of extra-solar planets. The TMT will operate over a 0.3- to $30\text{-}\mu\text{m}$ wavelength range, providing 9 times the collecting area of the current largest optical telescope, the 10-m Keck Telescope. It will use an adaptive optics system to allow diffraction-limited performance, resulting in spatial resolution 12.5 times sharper than is achieved by the Hubble Space Telescope. For more about the TMT, see [62].

G. The Multiple Mirror Telescope

The Multiple Mirror Telescope (MMT) is a joint project of the University of Arizona and the Smithsonian Institution. Located on Mount Hopkins, Arizona, the MMT is a 6.5-m optical telescope used for spectroscopy, wide-field imaging, and adaptive optics astronomy.

Several advances in telescope design were pioneered at the MMT. Among these are a compact, altitude-azimuth structure with a co-rotating building, in-situ aluminization of the primary mirror, and adaptive optics with deformable secondary mirrors and artificial guide stars.

The MMT was first designed as a multiple-mirror telescope, with six 1.8-m primary mirrors in a single mount. Automated alignment of the individual light paths gave the telescope an equivalent aperture of 4.5 m, with a 6.9-m baseline for interferometry. The recent upgrade created a new 6.5-m-class telescope, although significant challenges remain in improving the telescope performance in pointing and tracking, because the structural behavior of the new telescope is not completely understood and the control system is in the process of being re-designed. (See the MMT web site [63].)

III. Control System Structure

A typical antenna is moved in the azimuth (vertical) axis and the elevation (horizontal) axis. The movements are independent, and their control systems are independent as well. Due to the independence, in the following we will consider a single axis only.

An antenna control system consists of the rate and position feedback loops, as shown in Fig. 2. The rate loop includes the antenna structure and the drives. The drive (motor) rate is fed back to the rate controller. Typically, the rate loop is designed such that the antenna steady-state rate is proportional to

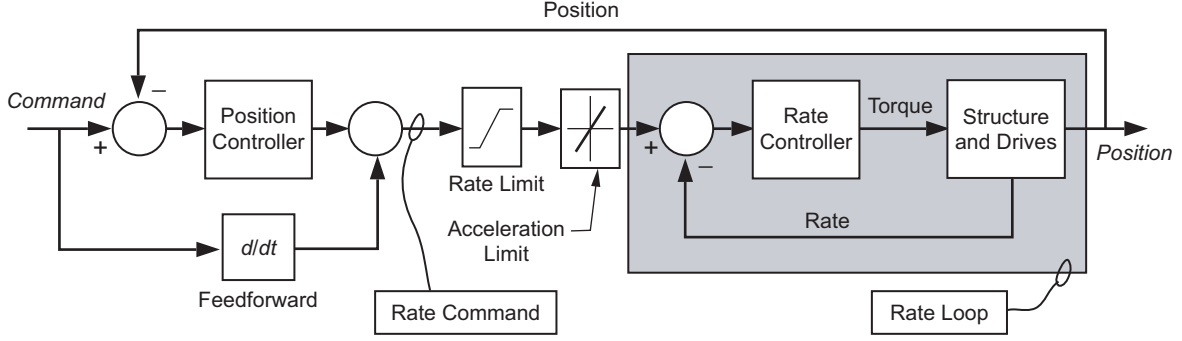


Fig. 2. Antenna control system.

the constant rate-loop input; the latter is called the rate command. The antenna position is measured with the azimuth and elevation encoders. The position loop is an outer loop that feeds back the antenna position.

The antenna rate and acceleration are limited (see Fig. 2), and the limits reflect the restricted power of the antenna drives. During tracking, the limits are not violated; however, the rate and acceleration limits are hit during antenna slewing.

IV. Control System Models

Antenna control system models are indispensable in the antenna controller design and implementation stages for two reasons. In the design stage, they are used to determine the controller gains and to assess the control system performance; in the implementation stage, the models are part of the antenna controllers and help to fine-tune the antenna pointing precision.

In the design stage, an analytical model of the control system is developed. It includes the finite-element model of a structure, motor and gearbox models, amplifiers and filters, and also nonlinearities: friction, backlash, and rate and acceleration limits. An example of such a model is given in [3,4]; a drive system model is given in [5,6].

In the implementation stage, the antenna model is obtained from the open-loop antenna field tests, using a system identification procedure. The model accuracy is particularly important when the antenna controller is a model-based controller, such as a linear quadratic Gaussian (LQG) or H_∞ controller.

In order to obtain the model, an antenna is excited with white noise (a noise is “white” if its bandwidth is much wider than the bandwidth of the open-loop antenna), and the encoder output is recorded. From the input and output records, the transfer function is obtained [1,7]; an example of the azimuth transfer function of the 34-m antenna is shown in Fig. 3 (dashed line). From the input-output data, the system state-space model is identified. In Fig. 3, the magnitude of the transfer function obtained from the identified state-space model is shown (solid line). The magnitude of the transfer function consists of the rigid body part that dominates lower frequencies (below 1 Hz) and is characterized with the -20 dB/dec slope. At higher frequencies—above 1 Hz—the transfer function shows flexible deformations characterized by resonant peaks. One can find information on the development of the control system based on the identified model in [1,8]; see [9] for information on telescope identification using a swept-sine generator and [10] on the Galileo Telescope model identification.

The antenna azimuth model depends on the antenna elevation position. Note, for example, that an antenna with its dish at zenith has different structural properties than the antenna with its dish pointed horizontally. Figure 4 shows the measured magnitudes of the azimuth transfer functions for a

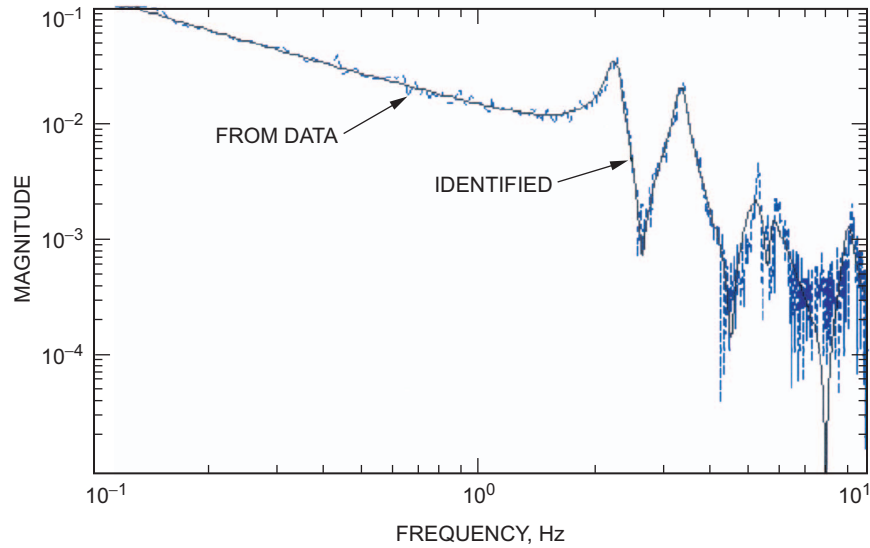


Fig. 3. Magnitude of the transfer function of the 34-m DSN antenna.

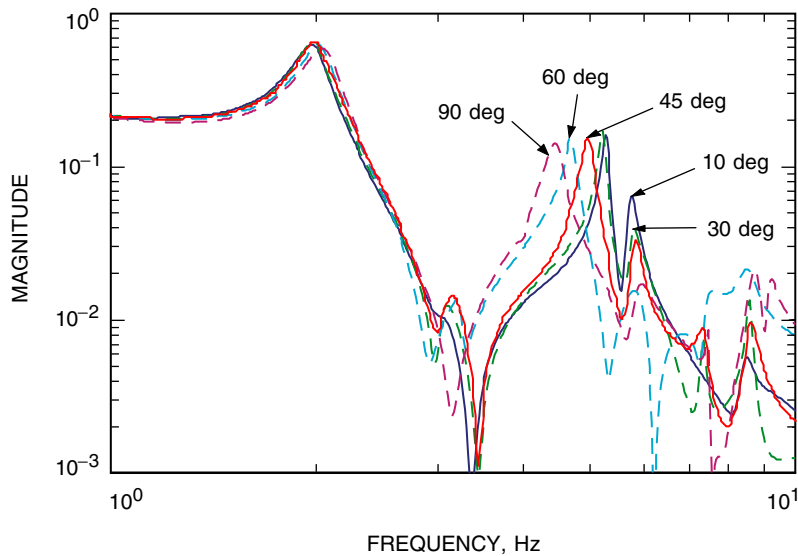


Fig. 4. Magnitude of the azimuth transfer function of the 34-m DSN antenna for different elevation angles (DSS 26, azimuth rate-loop models, data collected in April 1997).

34-m antenna at different elevation positions. The variations of the first two natural frequencies with respect to the antenna elevation position are shown in Fig. 5. From these figures, we see that the natural frequencies depend on the antenna elevation position: the second frequency changes significantly with the elevation angle.

Antenna natural frequencies depend also on the antenna size. It is a general tendency that the natural frequencies decrease with an increase of the antenna size (the structure becomes “softer”). The lowest natural frequency (called the fundamental frequency) is considered a measure of compliance of the structure. The Aerospace Corporation collected data on the fundamental frequencies of many antenna structures. In these data, the tendency of frequencies to decrease with an increase of antenna dish size

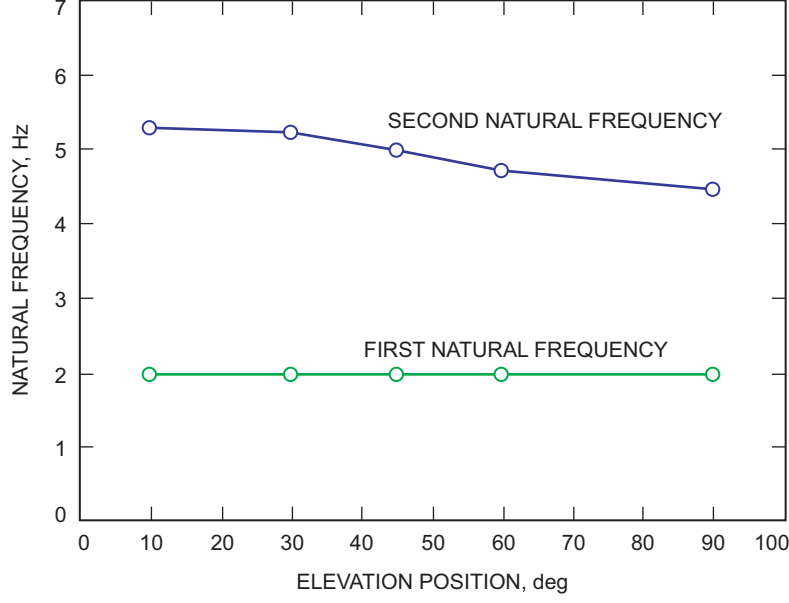


Fig. 5. The variation of the two first natural frequencies of the antenna structure as a function of its elevation position.

is observed. Based on these data, we determined the best-fit line (in logarithmic scale) defined by the following equation:

$$f = 20.0d^{-0.7} \quad (1)$$

The line is presented in Fig. 6. In the above equation, d is antenna diameter in meters and f is the antenna fundamental (lowest) frequency in hertz. This equation represents the average natural frequency for a given antenna diameter. Equation (1) allows for evaluation of the structural soundness of a particular antenna: if the fundamental frequency of the considered antenna structure is higher than the frequency obtained from Eq. (1), the structure is stiffer than average (thus of better pointing performance); if it is lower, the structure is softer than average (thus of inferior pointing performance).

V. Disturbance Model

The main antenna disturbance is wind. Wind gust spectra depend on the geographical location and on the terrain profile. Different spectra, based on wind gust measurements, are used to model wind gusts. We present here the Davenport spectrum, $S_v(\omega)$, that depends on average wind speed and terrain roughness as follows [11]:

$$S_v(\omega) = 4800v_m\kappa \frac{\beta\omega}{(1 + \beta^2\omega^2)^{4/3}} \quad (2)$$

where v_m is the mean wind speed, $\beta = 600/\pi v_m$, and κ is the surface drag coefficient, obtained from the roughness of the terrain; see [12], $\kappa = (2.5 \ln(z/z_o))^{-2}$. In the above equation, z is the distance from the ground to the antenna dish center, and z_o is the height of the terrain roughness (e.g., $z_o = 0.1$ to 0.3 m at Goldstone, California). For 34-m antennas, $z = 17$ m; thus, $\kappa = 0.006$ to 0.010 . The Davenport spectrum is shown in Fig. 7 (solid line).

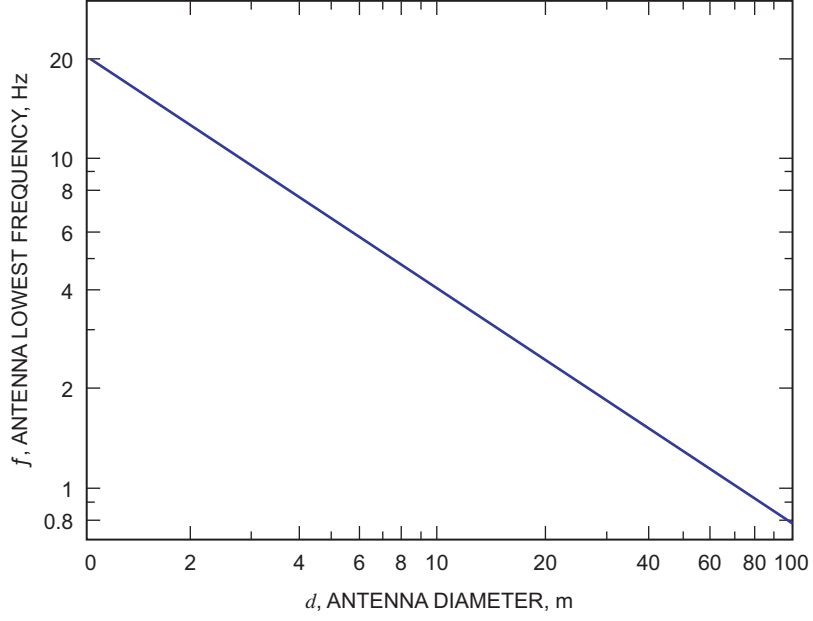


Fig. 6. The best-fit line that fits the Aerospace Corp. chart of antenna fundamental frequencies.

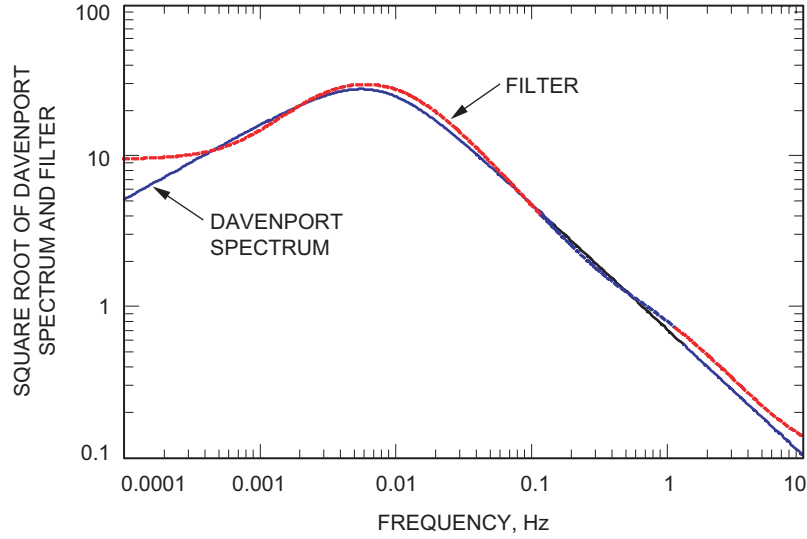


Fig. 7. The Davenport spectrum and its approximating filter.

In order to model wind gusts in the time domain, the spectrum is approximated with a linear filter. The filter was obtained in [13] by adjusting the filter parameters such that the magnitude of the filter transfer function best fits the Davenport spectrum within the antenna bandwidth of $[0.001, 20]$ Hz. The resulting digital filter transfer function for a sampling time of 0.02 s is as follows:

$$G_w = \frac{0.1584z^3 - 0.3765z^2 + 0.2716z - 0.0534}{z^4 - 2.9951z^3 + 3.0893z^2 - 1.1930z + 0.0988} \quad (3)$$

The plot of the magnitude of the filter transfer function is shown in Fig. 7. A sample of the wind speed generated by the filter is shown in Fig. 8.

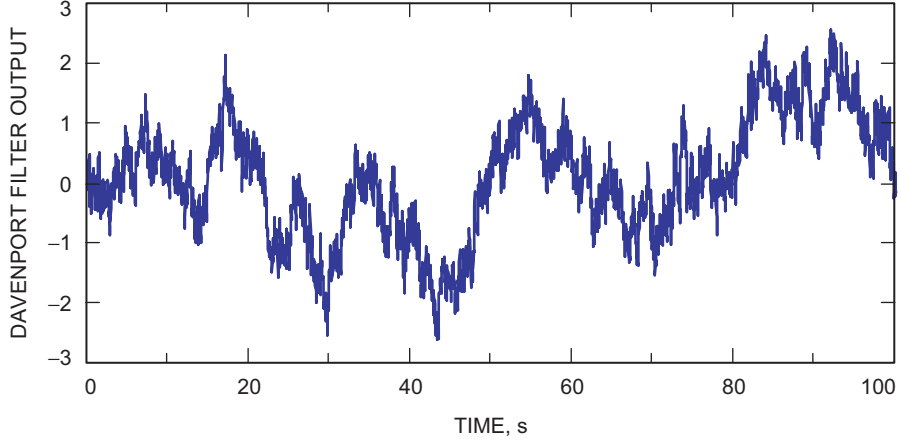


Fig. 8. The wind gust time history obtained from the Davenport filter.

Having the wind speed, the wind force is obtained (in newtons) as follows:

$$F_w(t) = k_f \Delta v(t) \quad (4)$$

where $k_f = 0.000892v_m^2$ and v_m is the wind mean speed, m/s; see [14]. See [15] on the Gemini Telescope wind model, [16] on steady-state wind modeling, and [17] on wind simulations.

VI. Position Controllers

We present an antenna performance with proportional-integral (PI), LQG, and H_∞ position controllers. See [18] on the application of a predictive controller to antenna control and [19] on periodic disturbance rejection.

A. Antenna Performance with a PI Controller

Consider the proportional (P) and integral (I) actions independently. Assuming a zero integral gain, $k_i = 0$, and the proportional gain $k_p = 0.5$, the response of the closed-loop system to a 10-mdeg step command is shown in Fig. 9(a). It has no overshoot and a settling time of 7 s. The response to a 10-mdeg/s rate offset has a constant servo error (or lagging) of 20 mdeg; see Fig. 9(b). The lag can be reduced by increasing the proportional gain. Indeed, increasing the gain to 1.6 produces a 6-mdeg lag; note, however, that the system is almost unstable—see the step response in Fig. 9(a). Thus, the proportional controller cannot completely eliminate the lagging.

The integral gain eliminates the lagging. A simulation of the antenna response to the 10-mdeg/s rate offset (with proportional gain $k_p = 0.5$ and integral gain $k_i = 0.1$) is shown in Fig. 10. Indeed, the rate-offset response has zero steady-state error as a result of the action of the integrator (for non-zero steady-state error, the integral of the error grows indefinitely, causing strong controller action). On the other hand, the integrator of the PI controller produces an overshoot; see Fig. 9(a).

The response of the PI controller to a 10-mdeg/s disturbance step, shown in Fig. 9(b), is slow and of large amplitude. The servo error in 10-m/s wind gusts is quite large: 5.8 arcsec; see Table 1. The variable-structure PI controller was described in [20].

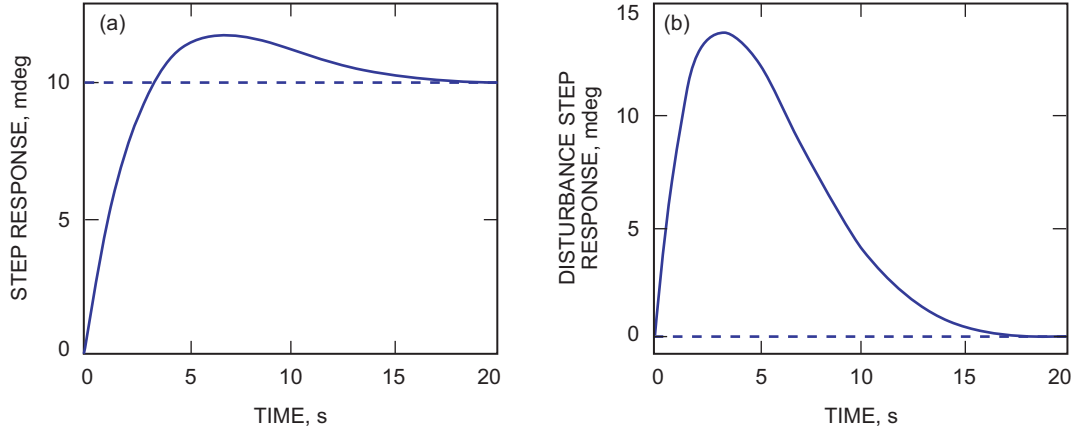


Fig. 9. Antenna performance with the PI controller: (a) response to 10-mdeg step command and (b) response to unit disturbance step.

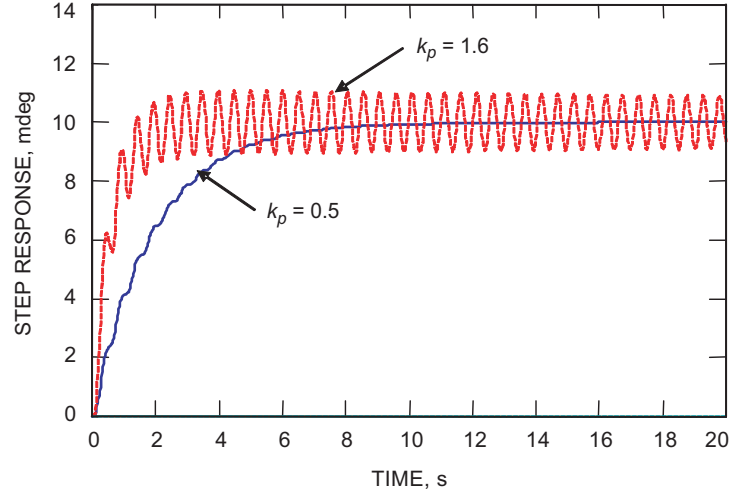


Fig. 10. Limits of performance of the PI controller.

Table 1. RMS servo error in 10-m/s wind gusts.

Controller	Azimuth servo error, arcsec	Elevation servo error, arcsec
PI	1.8 ^a	5.8 ^a
LQG	0.10	0.39
H _∞	0.08	0.18

^a From measurements; see [21].

B. Antenna Performance with a Feedforward Controller

The feedforward loop is added to improve tracking accuracy at high rates [2]. In this loop, the command is differentiated and forwarded to the rate-loop input; see Fig. 2. The derivative is an approximate inversion of the rate-loop transfer function. In this way, we obtain the open-loop transfer function from the command to the encoder, approximately equal to 1. Indeed, the magnitude of the rate-loop transfer function G_r is shown in Fig. 11. It is approximated (up to 1 Hz) with an integrator ($G_{rapprox} = 1/s$), shown in the same figure (dashed line). The feedforward transfer function is a derivative ($G_{ff} = s$), shown in Fig. 11 (dashed-dotted line), so that the overall open-loop transfer function is a series of the feedforward and the rate loop $G_o = G_r G_{ff}$, which is approximately equal to 1 up to the frequency 1 Hz. The position feedback is added to compensate disturbances and system imperfections.

C. Antenna Performance with an LQG Controller

It has been noted that the bandwidth, the speed of the system response, and the disturbance-suppression abilities of the PI controller improve with the increase of the controller proportional gain (up to a limiting value at which the antenna vibrates). If the vibrations could be sensed and controlled, the performance could be further improved. The encoder is the antenna position sensor. The Fourier transformation of the encoder measurements shows antenna vibrations, indicating that the antenna vibrations can be recovered from the encoder data. This can be done using an estimator, as in Fig. 12. The estimator is an analytical antenna model driven by the same input as the antenna itself and by the estimation error (the difference between the actual encoder reading and the estimated encoder reading). The error is amplified with the estimator gain k_e to correct for transient dynamics (Fig. 12). The estimator returns the antenna states that consist of the estimated encoder reading (or noise-free encoder measurements) and the estimated states x_f of the flexible deformations of the antenna structure. The latter states effectively replace the missing vibration measurements. The resulting controller's output is a combination of the PI controller output and the flexible-mode controller output. The first takes care of the tracking motion; the latter suppresses the antenna vibrations. In the above configuration,

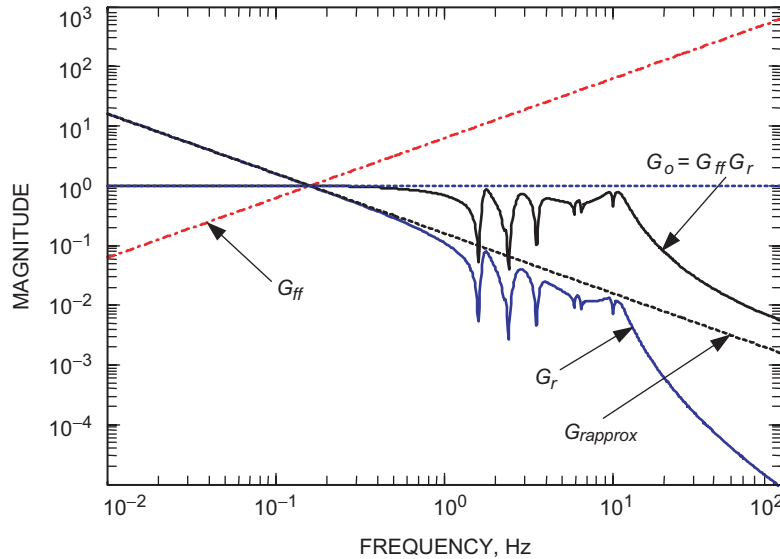


Fig. 11. The feedforward action is illustrated with the magnitudes of the transfer functions (G_r is the rate-loop transfer function, $G_{rapprox}$ is the rate-loop transfer function approximation, G_{ff} is the feedforward loop transfer function, and $G_o = G_{ff} G_r$ is the transfer function of the series connection of the feedforward and rate loops).

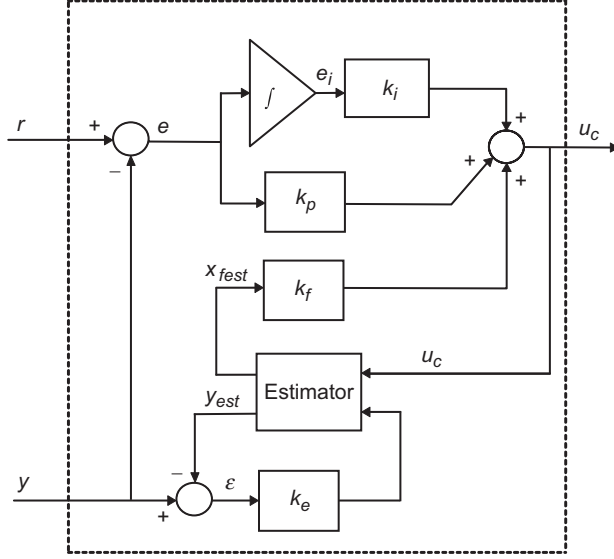


Fig. 12. The LQG controller structure.

the increased proportional-and-integral gains do not destabilize the closed-loop system, since the flexible-mode controller keeps the antenna vibrations suppressed. If the gain determination procedure minimizes the so-called LQG index, the controller is called an LQG controller. One can find the description of the LQG controller design in [1,7], and a design tool is described in [22]. The application of the LQG controller to a 20-m radio telescope is described in [23].

The performance of the LQG controller designed for a 34-m antenna is illustrated in Fig. 13(a) (the response to a 10-mdeg step command) and Fig. 13(b) (the response to a 10-mdeg/s disturbance step). The step response has a small settling time of 2 s, and the disturbance step response has a low magnitude of short duration (2 s). The rate offset shows zero lagging. The servo error in 10-m/s wind gusts is small: 0.10 arcsec (Table 1). These parameters show that the LQG controller is of an order better than the PI controller.

D. Antenna Performance with the H_∞ Controller

H_∞ controllers outperform LQG controllers in many applications. The structure of an H_∞ controller is similar to that of the LQG controller, but its parameters are obtained from a different algorithm. While the LQG controller minimizes the system H_2 norm (its rms response to the white noise input), the H_∞ controller algorithm minimizes the system H_∞ norm (in the case of a single-input–single-output system, the system H_∞ norm is the maximal magnitude of its transfer function).

The antenna H_∞ controller was designed by shaping the disturbance input. A filter of the Davenport wind spectrum profile was used as a shaping (or weighting) factor. The H_∞ controller design for antenna tracking purposes is described in [1,24]. The performance of the antenna is shown in Fig. 14. The figures show very small settling time (1.2 s) and small overshoot (less than 10 percent). These features significantly exceed LQG controller performance. The response to the 10-mdeg/s rate offset has zero steady-state error. The servo error in 10-m/s wind gusts is small: 0.08 arcsec (see Table 1). The application of the H_∞ controller to the airborne telescope SOFIA is described in [25], to the Thirty Meter Telescope in [26], to a segmented-mirror telescope in [27,28], and to the secondary mirror of a Giant Segmented Mirror Telescope in [29].

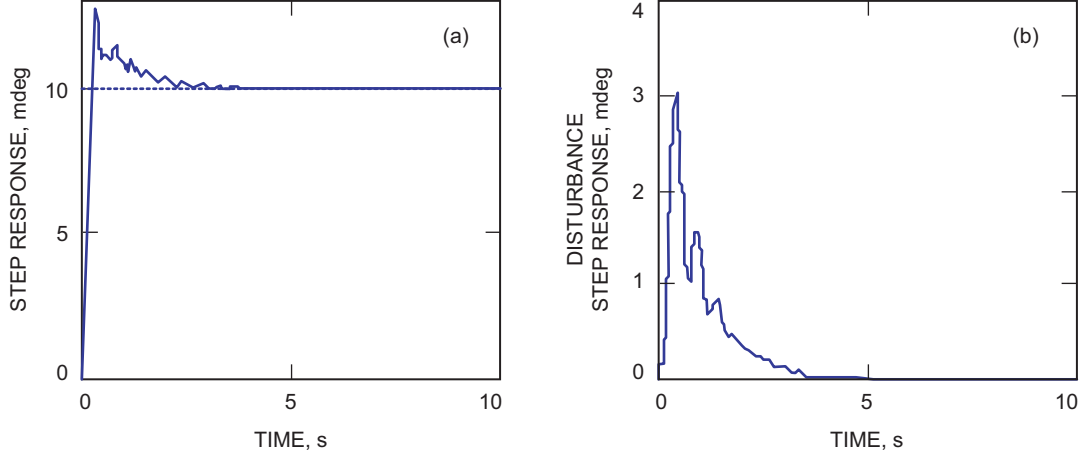


Fig. 13. Antenna performance with the LQG controller: (a) response to 10-mdeg step command and (b) response to unit disturbance step.

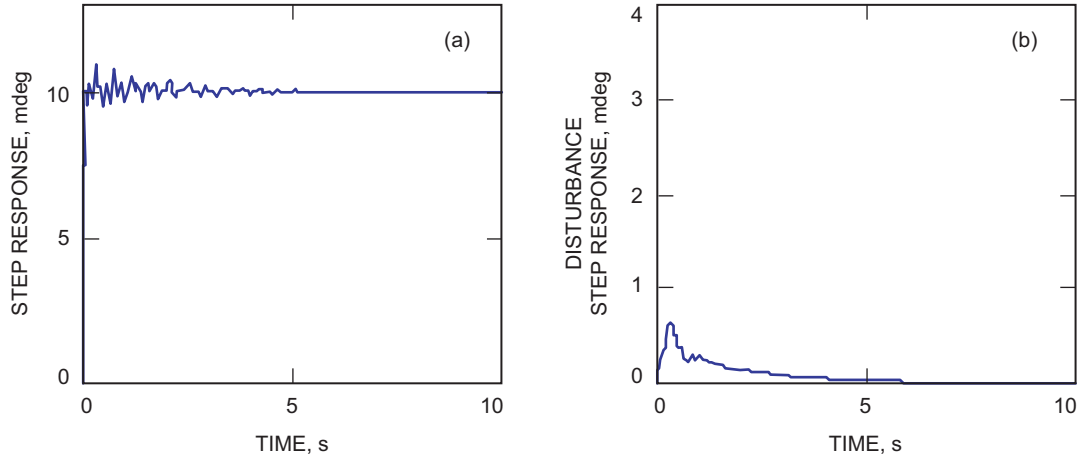


Fig. 14. Antenna performance with the H_∞ controller: (a) response to 10-mdeg step command and (b) response to unit disturbance step.

VII. Command Preprocessor

When an LQG or H_∞ controller is implemented, it initiates limit cycling during antenna-slewing operations. This phenomenon is caused by the antenna rate and acceleration limits: the controllers are designed for a linear plant, while limits cause antenna non-linear dynamics. In order to avoid the cycling, one can either apply different controllers for tracking purposes and for slewing or implement an anti-windup technique (see [30]), or apply a controller with variable gains [20,31], or use a trajectory calculated in advance, such that it never exceeds the rate and acceleration limits [32], or use a command preprocessor (CPP). This article presents the latter approach. The preprocessor is a computer program that generates a modified command, identical with the original one, if the rate and accelerations are within the limits, and a command of maximal (or minimal) rate and acceleration when the limits are met or violated. The location of the preprocessor in the antenna control system is shown in Fig. 15.

The block diagram of the CPP is shown in Fig. 16. It imitates a rigid antenna (represented by the integrator) driven by a variable-gain controller with a feedforward gain (the latter represented by the derivative). The variable gain k_i depends on the preprocessor error e_i as follows:

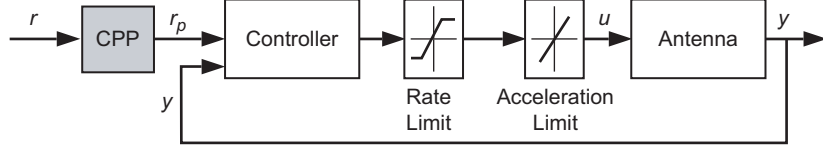


Fig. 15. The CPP location in the antenna control system.

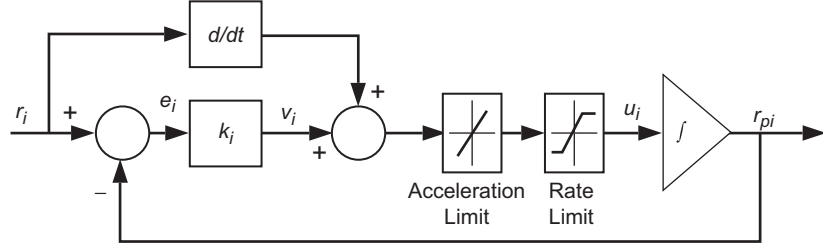


Fig. 16. The CPP block diagram.

$$k_i = k_o + k_v e^{-\beta |e_i|} \quad (5)$$

In this equation, k_o is the constant part of the gain, k_v is the variable part of the gain, and β is the error exponential. The plot of $k_i(e_i)$ for $k_o = 1$, $k_v = 5$, and $\beta = 20$ is shown in Fig. 17. The detailed description of the CPP is given in [12].

The CPP response to a step of 10 deg is shown in Fig. 18. The preprocessed command begins with the maximal acceleration until it reaches the maximum rate, and then continues with the maximal (and constant) rate, and finally slows down with the minimal deceleration. After reaching a value of 10 deg, the error between the original and the preprocessed command is zero.

The measured responses of the antenna to a large (non-processed) step input of 10 deg are shown in Fig. 19(a). Clearly, an unstable limit cycling is present. The same response of the antenna with a processed command is shown in Fig. 19(b), where the antenna follows closely the processed command, without limit cycling.

VIII. Pointing Error Sources

The following is a list of the main pointing error sources that are not detectable by the antenna sensor encoders:

- (1) The antenna encoders are not co-located with the RF beam; thus, the beam position is measured with a certain bias.
- (2) The antenna control torques are applied at the motor locations, while the wind disturbances are distributed over the antenna surface; thus, only a certain portion of the disturbances can be compensated with the motors.
- (3) Disturbances: Thermal and wind forces are the main sources of disturbances and are difficult to measure. Gravity forces and azimuth track imperfections are measurable and repeatable disturbances. Atmospheric refraction is a measurable but unrepeatable disturbance.

- (4) Model uncertainty: Manufacturing imperfections and the variable antenna configuration (its structural properties depend on its elevation angle) are the sources of uncertainty that limit the controller performance.
- (5) Nonlinearities: Backlash and friction torques at the antenna drives, rate, and acceleration limits are the main sources of nonlinearity.

The pointing error sources and corrections for the Green Bank telescope are presented in [33]; for active corrections of structural deformations, see [34]; for tracking performance, see [35]; on use of inclinometers for measuring telescope position, see [36]; and on thermal and wind control of the European Southern Observatory (ESO) Very Large Telescope, see [37].

A. Azimuth Track Imperfections

The antenna rotates in the azimuth on a circular azimuth track, which is manufactured with a level precision of ± 0.5 mm for the 34-m DSN antennas. The uneven azimuth track level causes antenna tilts and flexible deformations. The finite-element model of the alidade (lower antenna structure) deformations due to track unevenness is shown in Fig. 20. Certainly, these deformations impact antenna pointing accuracy. However, the pointing errors caused by the track irregularities are repeatable; therefore, they can be calibrated. By developing a look-up table, one provides pointing corrections as a function of the antenna azimuth position. The look-up table is generated by using inclinometers that measure tilts of the alidade structure at selected points.

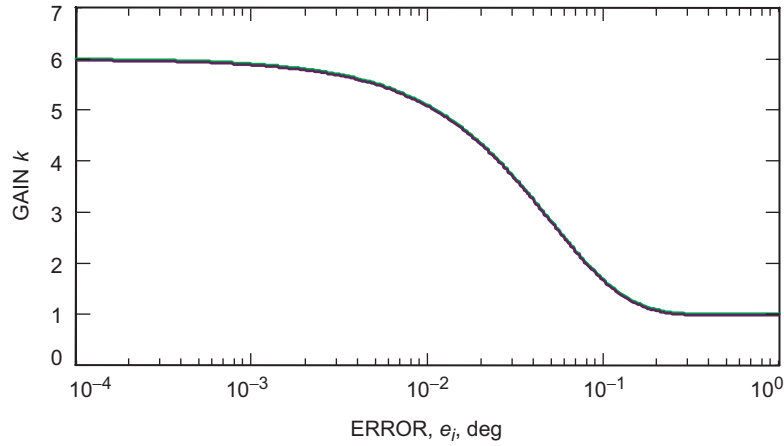


Fig. 17. The CPP gain versus CPP error.

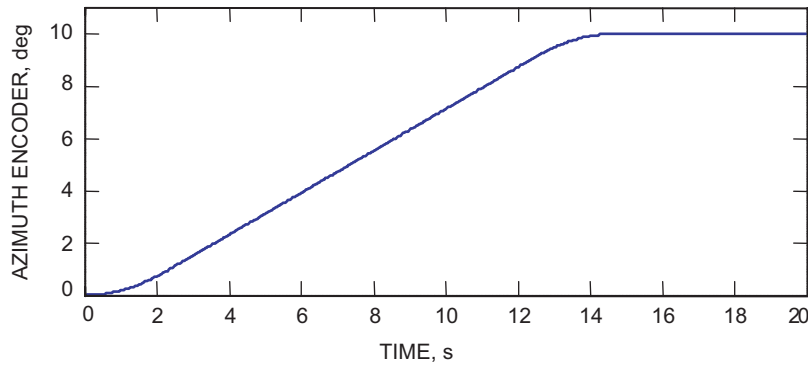


Fig. 18. The CPP response to a 10-deg step.

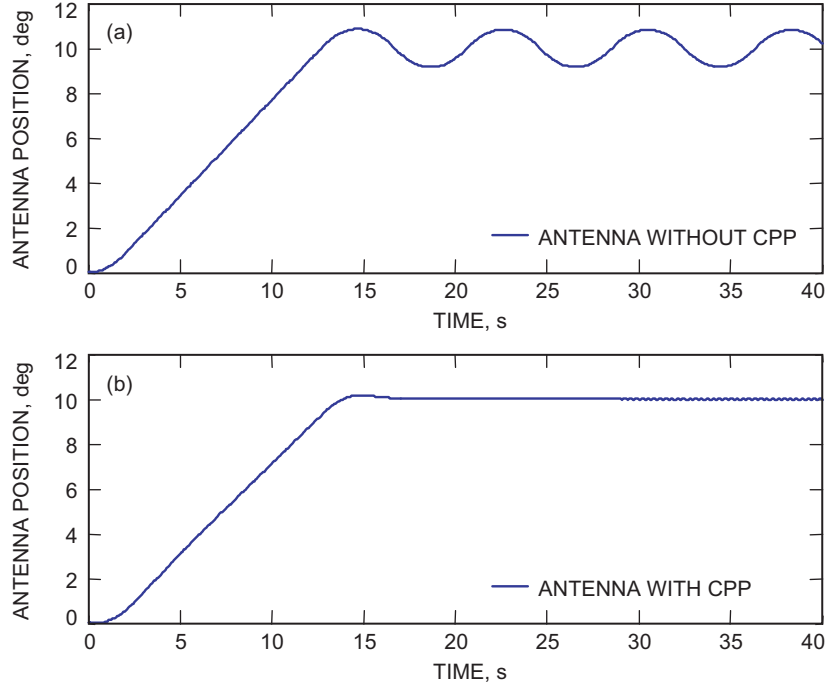


Fig. 19. Antenna response to a 10-deg step: (a) without CPP and (b) with CPP.

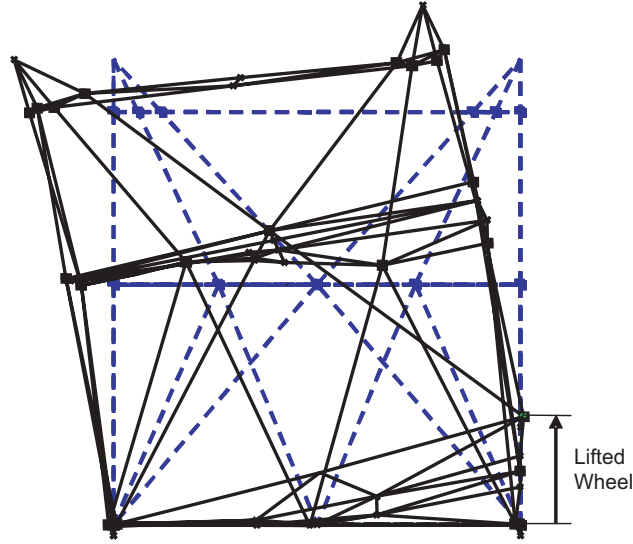


Fig. 20. Alidade deformation due to wheel lift.

Four inclinometers were installed on the alidade structure, at locations marked in Fig. 21. Each inclinometer measures tilts of its x- and y-axes. The locations of the inclinometers were selected such that their tilts estimate the alidade elevation and cross-elevation rotations at the antenna focal point. Inclinometers no. 1 and no. 2 are located at the top of the alidade. Inclinometer no. 2 is located next to the elevation encoder. The y-axis tilt of this inclinometer reflects the elevation pointing error. Inclinometers no. 3 and no. 4 are located in the middle of the crossbeam of the left and right sides of the alidade, respectively. Their x-axis tilts combined with the x-axis tilts of inclinometers no. 1 and no. 2 give the cross-elevation pointing error, as shown below.

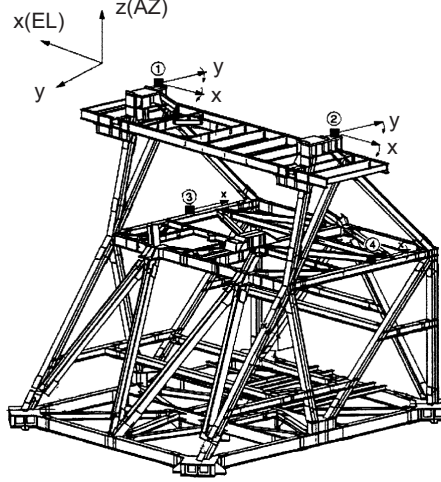


Fig. 21. Alidade and the inclinometer locations.

The x- and y-axis tilts of the i th inclinometer are denoted α_{ix} and α_{iy} , respectively. The inclinometer data were collected during the antenna azimuth rotation at a constant rate of 50 mdeg/s and a sampling frequency of 2 Hz. The tests were performed during nighttime to minimize deformations of the antenna structure due to the thermal gradient. The data show satisfactory repeatability.

The antenna elevation error Δ_{el} is the y-tilt of the second inclinometer:

$$\Delta_{el} = \alpha_{2y} \quad (6)$$

The cross-elevation error, Δ_{xel} , depends on the antenna elevation position, θ , and on the rotation, δ_y , of the top of the alidade with respect to the y-axis (tilt of the elevation axis) and the alidade twist, δ_z (the rotation of the top of the alidade with respect to the z-axis):

$$\Delta_{xel} = \delta_z \cos(\theta) - \delta_y \sin(\theta) \quad (7)$$

The tilt of the elevation axis is an average of the x-tilts of inclinometers no. 1 and no. 2, that is,

$$\delta_y = 0.5(\alpha_{1x} + \alpha_{2x}) \quad (8)$$

while the alidade twist is determined from x-tilts of inclinometers no. 3 and no. 4,

$$\delta_z = \frac{h}{l}(\alpha_{7x} - \alpha_{8x}) \quad (9)$$

where h is the alidade height and l is the distance between the inclinometers. The details are in [38].

The reading of inclinometer no. 1, x-axis, is shown in Fig. 22. The fitted sinusoid shows the azimuth axis tilt. The pointing error obtained from the inclinometer measurements is shown in Fig. 23 (solid line). The measurements of the actual pointing error (using the conical scan (conscan) technique) are shown in the same figure (with dots). The figure shows the coincidence of the inclinometer and conscan data.

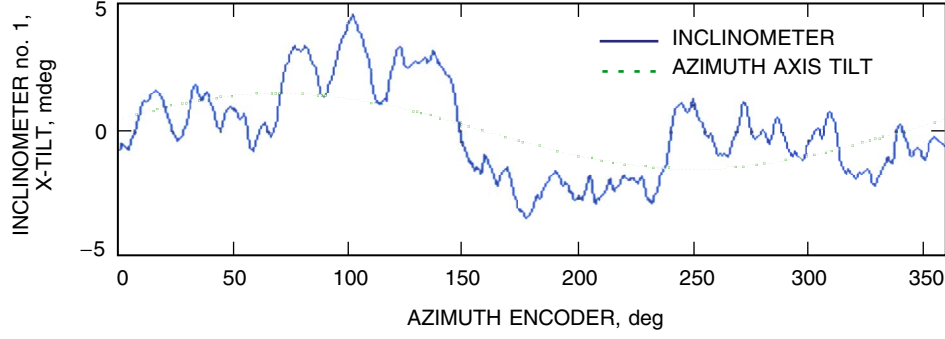


Fig. 22. Inclinator no. 1 tilt, x-direction.

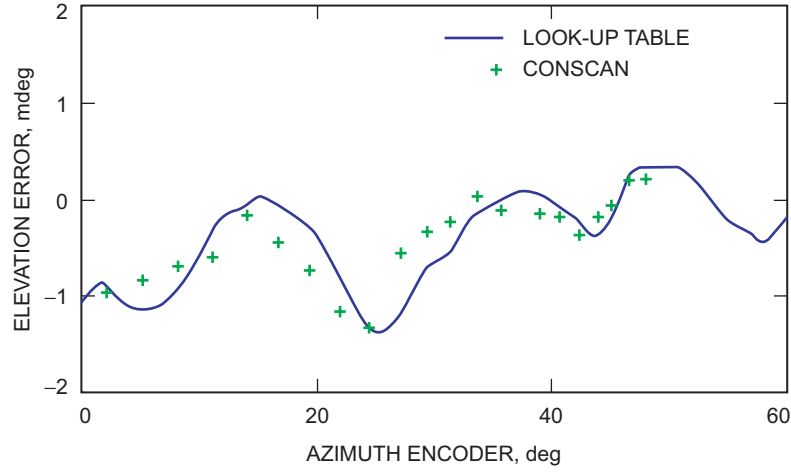


Fig. 23. Antenna tilts due to track level unevenness: from the look-up table and measured by conscan.

B. Thermal Deformations

The temperature gradient causes deformations of the antenna structure—thus, it impacts the pointing accuracy. The inclinometers were used to measure antenna tilts when the antenna was stowed. A sample shown in Fig. 24 shows tilts of 8 mdeg. The largest tilts were in the afternoons, when the sun heat was intensive (although the data were collected in November, which is not the hottest month at the Mojave Desert, where the antennas are located). See [37,39,40] on techniques to compensate for the thermal deformations.

C. Gravity Deformations

Gravity forces deform the antenna dish and subreflector, and the deformations depend on the dish elevation position. These deformations are repeatable and can be calculated comparatively accurately using the finite-element model. The gravity deformations of the 70-m antenna are shown in Fig. 25. The calculated deformations allow one to generate a look-up table of the pointing corrections.

D. Atmospheric Refraction

The RF beam is bent while passing through the atmosphere (see Fig. 26). The amount of refraction depends on air humidity and can be calculated. The atmospheric conditions are monitored by weather stations, and a refraction model calculates the correction once a second. The refraction corrections are added to the antenna pointing model, and they can be on the order of several hundred millidegrees.

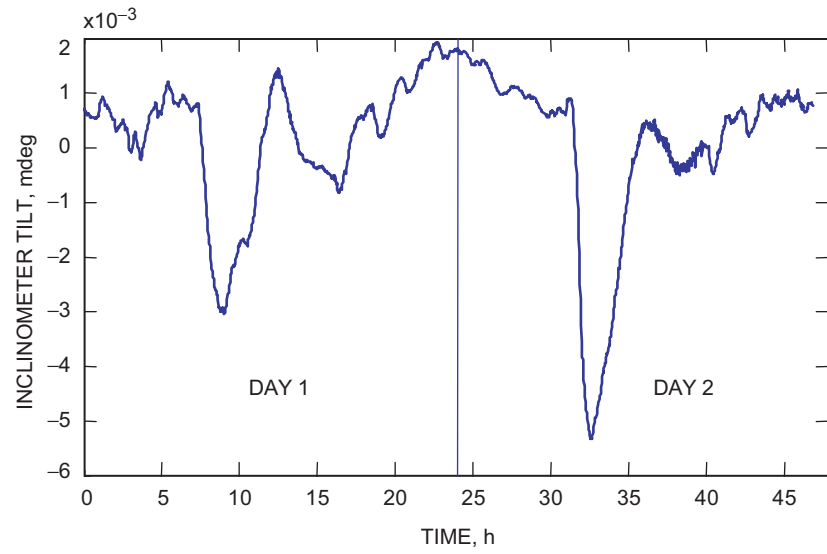


Fig. 24. Thermal deformations of the 34-m DSN antenna.

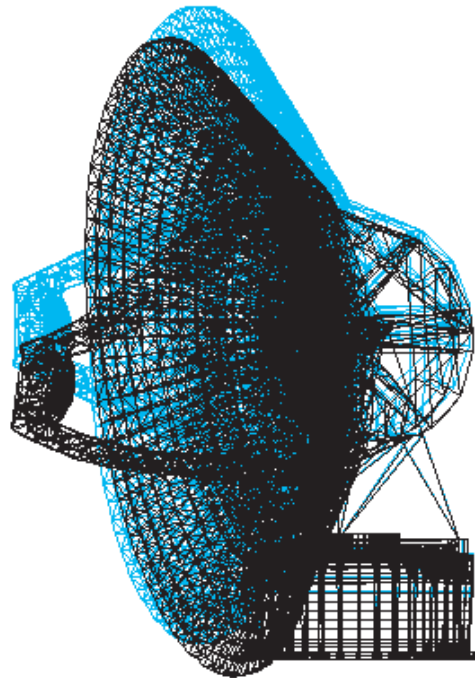


Fig. 25. Gravity deformation of the 70-m antenna.

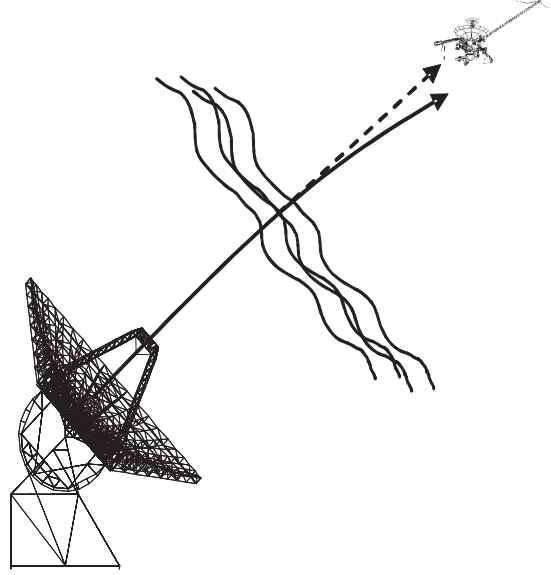


Fig. 26. Atmospheric refraction.

E. Friction

Antenna/telescope drive friction can cause pointing errors. In order to improve pointing, the best thing is to reduce the friction. For example, the 70-m DSN antennas use oil film to rotate in azimuth. Machine jackscrews, often used in elevation drives, are sources of significant friction. When friction cannot be reduced through structural modifications, control engineering tools are implemented. One of them is dither, i.e., oscillations applied at the friction source to break the friction contact. The dither frequency should be higher than the antenna structural frequencies to avoid excitation of structural resonances. An analysis of dither as applied to the antenna is given in [41]. The friction modeling of the 2.5-m telescope is described in [42]; for more on friction compensation, see [43–45].

F. Backlash

Gearboxes and gears are antenna drive components. A backlash phenomenon at the gearboxes is observed when one gear rotates through a small angle without causing a corresponding movement of the second gear. This causes beating in the drives, gear wear, and deterioration of antenna tracking precision. In order to maintain antenna pointing precision, the backlash phenomenon is eliminated by implementing two symmetric drives with a specific torque difference between them (see Fig. 27). The torque difference is called a torque bias, or counter-torque. With two-motor configurations, the backlash clearance will occur at one drive while the other is still coupled. The antenna dynamics will be controlled by the latter drive. The effectiveness of the two-motor approach depends on the amount of torque bias applied at the drives, which depends on the antenna variable load. The torque bias should be large enough to lead the antenna through the gap for the maximal allowable torque load, but small enough that it will not cause excessive local stress, friction, or wear. For more on backlash, see [46–53].

IX. Pointing-Error Correction

A. Look-up Tables

Look-up tables are used to correct for the known and repeatable errors (e.g., gravity deformations, azimuth track level corrections). For non-repeatable errors, an additional feedback (e.g., conscan or monopulse) is applied.

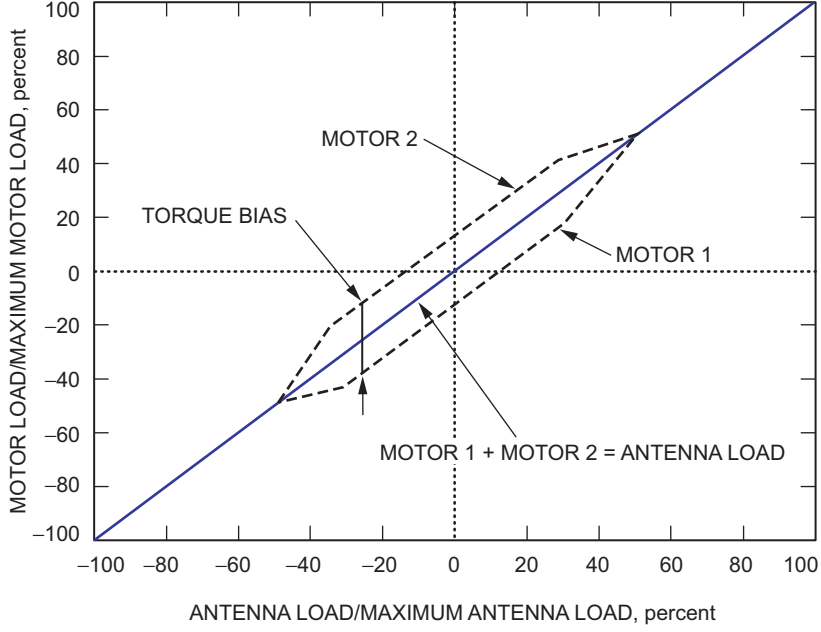


Fig. 27. Motor torques and the counter-torque.

B. Conical Scan (Conscan)

Conscan is an additional feedback. This technique is commonly used for the determination of the true spacecraft position. During conscan, circular movements are added to the antenna command, as shown in Fig. 28. The circular movements cause sinusoidal variations of the power of the signal received from the spacecraft, as illustrated in Fig. 29. The power variations are used to estimate the true spacecraft position. The time of one cycle is between 30 and 60 s; thus, the correction update is comparatively slow. The drawback of this technique is that the antenna is always off the peak power, i.e., always slightly off the target.

The control system of the conscan consists of the additional (outer) feedback that corrects for the difference between the encoder and RF beam position (see Fig. 30). For more about conscan, see [54,55].

C. Monopulse

In this algorithm, the pointing error is estimated from RF signals received by the monopulse feed horn. These signals are uniquely related in amplitude and phase as a function of the antenna pointing error. The single monopulse feed design allows direct pointing at the target at all times, allowing for the spacecraft to be tracked at the peak of the antenna pattern. This technique is much faster than conscan (the updating time is 0.02 s). For more about monopulse, see [56,57].

X. Conclusions

This article presented the challenges that control system engineers encounter while trying to satisfy demanding pointing requirements. Not all challenges have satisfactory solutions. One of the reasons is the lack of a stable point of reference to measure the RF beam position. The substitute beam position measurements using encoders are subject to painstaking corrections, which do not always satisfy the requirements. A fast and inexpensive measurement system of beam position would be a breakthrough in antenna/telescope technology.

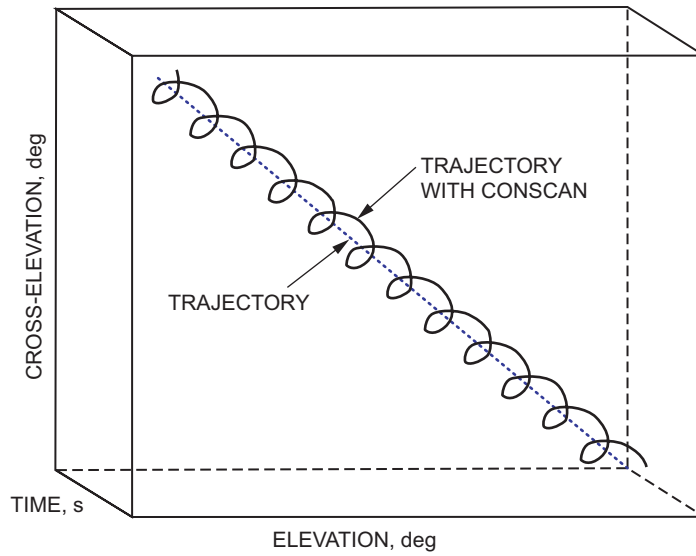


Fig. 28. Antenna trajectory when performing a conical scan.

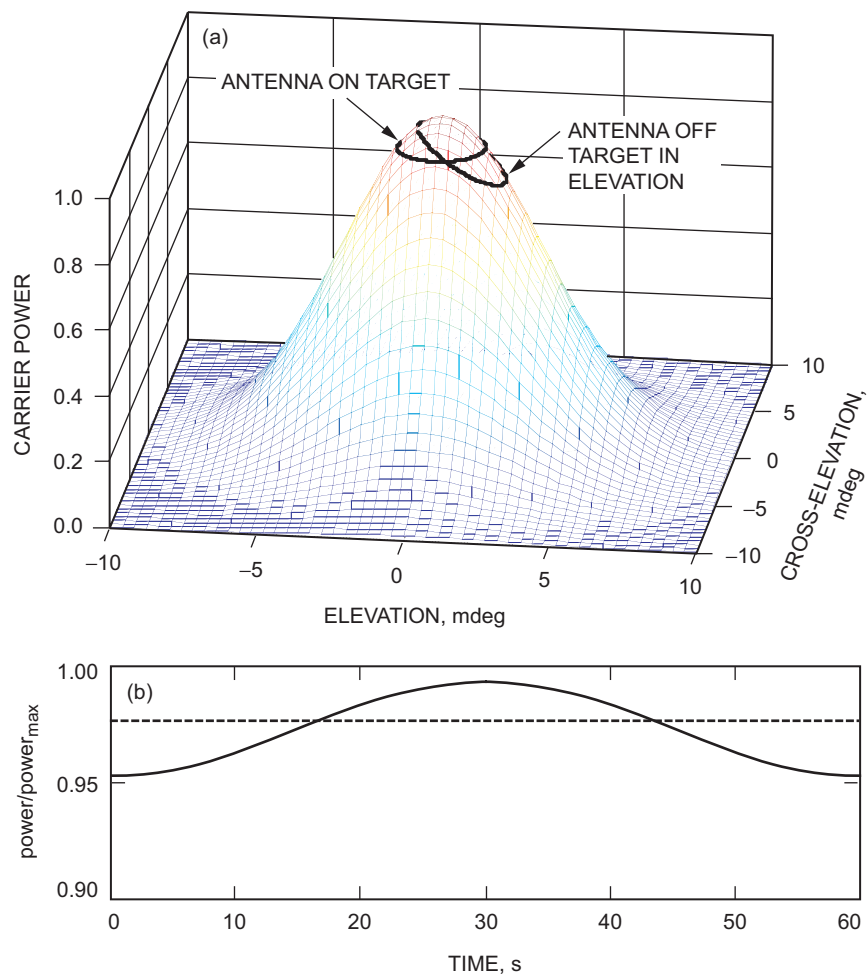


Fig. 29. Conscan: (a) antenna power and (b) power variation.

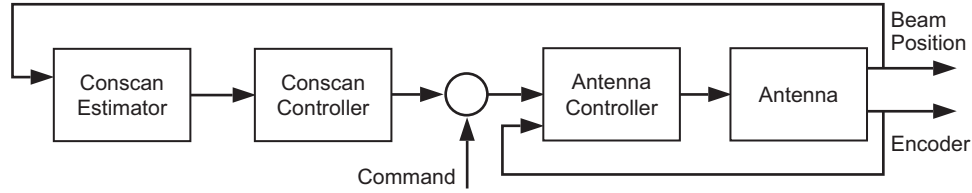


Fig. 30. Antenna conscan controller.

References

- [1] W. Gawronski, *Advanced Structural Dynamics, and Active Control of Structures*, New York: Springer, 2004.
- [2] W. Gawronski and J. A. Mellstrom, "Control and Dynamics of the Deep Space Network Antennas," chapter in *Control and Dynamic Systems*, vol. 63, ed., C. T. Leondes, San Diego, California: Academic Press, 1994.
- [3] W. Gawronski and K. Souccar, "Control System of the Large Millimeter Telescope," SPIE Astronomical Telescopes and Instrumentation Conference, Glasgow, United Kingdom, June 2004.
- [4] D. Clark "Control System Prototyping—A Case Study," Technical Memorandum ITM-04-3, MMT Observatory, Smithsonian Institution and The University of Arizona, www.mmto.org/MMTpapers/tech00_10.shtml#2004
- [5] T. Erm and P. Gutierrez, "Integration and Tuning of the VLT Drive Systems," *Proceedings of the SPIE, Telescope Structures, Enclosures, Controls, Assembly/Integration/Validation, and Commissioning*, vol. 4004, 2000.
- [6] S. Jimenez-Garcia, M. E. Magana, J. S. Benitez-Read, and J. Martinez-Carbalido, "Modeling, Simulation, and Gain Scheduling Control of Large Radiotelescopes," *Simulation Practice and Theory*, vol. 8, pp. 141–160, 2000.
- [7] W. Gawronski, C. Racho, and J. Mellstrom, "Application of the LQG and Feed-forward Controllers for the DSN Antennas," *IEEE Transactions on Control Systems Technology*, vol. 3, pp. 417–421, 1995; also see tmo.jpl.nasa.gov/tmo/progress_report/42-109/109R.PDF and tmo.jpl.nasa.gov/tmo/progress_report/42-112/112J.PDF
- [8] W. Gawronski, H. G. Ahlstrom, and A. M. Bernardo, "Analysis and Performance of the Control Systems of the NASA 70-Meter Antennas," *ISA Transactions*, vol. 43, 2004; also see tmo.jpl.nasa.gov/tmo/progress_report/42-144/144D.pdf
- [9] D. Clark, "Selected Results of Recent MMT Servo Testing," Technical Memorandum ITM-03-5, MMT Observatory, Smithsonian Institution and The University of Arizona, July 2003, www.mmto.org/MMTpapers/pdfs/itm/itm03-5.pdf
- [10] E. Cascone, D. Mancini, and P. Schipani, "Galileo Telescope Model Identification," *Proceedings of the SPIE*, vol. 3112, pp. 343–350, 1997.

- [11] E. Simiu and R. H. Scanlan, *Wind Effects on Structures*, New York: Wiley, 1978.
- [12] W. Gawronski and W. Almasy, "Command Pre-Processor for Radiotelescopes and Microwave Antennas," *IEEE Antennas and Propagation Magazine*, vol. 44, no. 2, pp. 30–37, 2002; also see
tmo.jpl.nasa.gov/tmo/progress_report/42-136/136A.pdf and
ipnpr.jpl.nasa.gov/tmo/progress_report/42-150/150G.pdf
- [13] W. Gawronski, B. Bienkiewicz, and R. E. Hill, "Wind-Induced Dynamics of a Deep Space Network Antenna," *Journal of Sound and Vibration*, vol. 178, no. 1, pp. 67–77, 1994; also see
tmo.jpl.nasa.gov/tmo/progress_report/42-108/108J.PDF
- [14] W. Gawronski, "Modeling Wind Gusts Disturbances for the Analysis of Antenna Pointing Accuracy," *IEEE Antennas and Propagation Magazine*, vol. 46, no. 1, pp. 50–58, 2004; also see
ipnpr.jpl.nasa.gov/tmo/progress_report/42-149/149A.pdf
- [15] G. Z. Angeli, M. K. Cho, M. Sheehan, and L. M. Stepp, "Characterization of Wind Loading of Telescopes," *Proceedings of the SPIE, Integrated Modeling of Telescopes*, vol. 4757, pp. 72–83, 2002.
- [16] W. Gawronski, J. Mellstrom, and B. Bienkiewicz, "Antenna Mean Wind Torques: A Comparison of Field and Wind Tunnel Data," *IEEE Antennas and Propagation Magazine*, vol. 46, 2004.
- [17] J. Mann, "Wind Field Simulations," *Prob. Engrg. Mech.*, vol. 13, pp. 269–282, 1998.
- [18] W. Gawronski, "Predictive Controller and Estimator for NASA Deep Space Network Antennas," *ASME Transactions, Journal of Dynamic Systems, Measurements, and Control*, no. 2, 1994; also see
tmo.jpl.nasa.gov/tmo/progress_report/42-104/104D.PDF
- [19] T. Erm and S. Sandrock, "Adaptive Periodic Error Correction for the VLT Telescopes," *Proceedings of the SPIE, Large Ground-Based Telescopes*, vol. 4837, paper 106, 2002.
- [20] D. Mancini, M. Brescia, E. Cascote, and P. Schipani, "A Variable Structure Control Law for Telescopes Pointing and Tracking," *Proceedings of the SPIE*, vol. 3086, 1997.
- [21] W. Gawronski, "Antenna Control Systems: From PI to H_∞ ," *IEEE Antennas and Propagation Magazine*, vol. 43, no. 1, pp. 52–60, 2001.
- [22] E. Maneri and W. Gawronski, "LQG Controller Design Using GUI: Application to Antennas and Radio-Telescopes," *ISA Transactions*, vol. 39, pp. 243–264, 2000; also see tmo.jpl.nasa.gov/tmo/progress_report/42-140/140D.pdf
- [23] M. Olberg, C. Lindeborg, A. Seyf, and C. F. Kastengren, "A Simple Robust Digital Controller for the Onsala 20m Radio Telescope," *Proceedings of the SPIE*, vol. 2479, pp. 257–265, 1995.
- [24] W. Gawronski, "An H_∞ Controller With Wind Disturbance Rejection Properties for the DSS-13 Antenna," *The Telecommunications and Data Acquisition Progress Report 42-127, July–September 1996*, Jet Propulsion Laboratory, Pasadena, California, pp. 1–15, November 15, 1996,
tmo.jpl.nasa.gov/tmo/progress_report/42-127/127G.pdf

- [25] U. Schoenhoff, A. Klein, and R. Nordmann, "Attitude Control of the Airborne Telescope SOFIA: μ -Synthesis for a Large Scaled Flexible Structure," *Proceedings of the 39th IEEE Conference on Decision and Control*, Sydney, Australia, 2000.
- [26] T. Erm, B. Bauvir, and Z. Hurak, "Time to Go H-Infinity?," *Proceedings of the SPIE, Advanced Software, Control, and Communication Systems for Astronomy*, vol. 5496, Glasgow, United Kingdom, 2004.
- [27] K. Li, E. B. Kosmatopoulos, P. A. Ioannou, and H. Ryaciotaki-Boussalis, "Large Segmented Telescopes: Centralized, Decentralized and Overlapping Control Designs," *IEEE Control Systems Magazine*, vol. 20, pp. 59–72, October 2000.
- [28] K. Li, E. B. Kosmatopoulos, P. A. Ioannou, H. Boussalis, and A. Chassiakos, "Control Techniques for a Large Segmented Reflector," *Proceedings of the 37th IEEE Conference on Decision and Control*, Tampa, Florida, 1998.
- [29] M. Whorton and G. Angeli, "Modern Control for the Secondary Mirror of a Giant Segmented Mirror Telescope," *Proceedings of the SPIE, Future Giant Telescopes*, vol. 4840, 2003.
- [30] Y. Peng, D. Vrancic, and R. Hanus, "Anti-Windup, Bumpless, and Conditioned Transfer Techniques for PID Controllers," *IEEE Control Systems Magazine*, vol. 16, no. 4, pp. 48–57, 1996.
- [31] D. Mancini, M. Brescia, E. Cascote, and P. Schipani, "A Neural Variable Structure Controller for Telescopes Pointing and Tracking Improvement," *Proceedings of the SPIE*, vol. 3112, 1997.
- [32] S. R. Tyler, "A Trajectory Preprocessor for Antenna Pointing," *The Telecommunications and Data Acquisition Progress Report 42-118, April-June 1994*, Jet Propulsion Laboratory, Pasadena, California, pp. 139–159, August 15, 1994, tmo.jpl.nasa.gov/tmo/progress_report/42-118/118E.pdf
- [33] J. J. Brandt, "Controlling the Green Bank Telescope," *Proceedings of the SPIE, Advanced Telescope and Instrumentation Control Software*, vol. 4009, 2000.
- [34] H. Baier, and G. Locatelli, "Active and Passive Microvibration Control in Telescope Structures," *Proceedings of the SPIE, Telescope Structures, Enclosures, Controls, Assembly/Integration/Validation, and Commissioning*, vol. 4004, 2000.
- [35] T. Erm, "Analysis of Tracking Performance," *Proceedings of the SPIE, Optical Telescopes Of Today And Tomorrow*, vol. 2871, pp. 1032–1040, 1996.
- [36] R. Kibrick, L. Robinson, V. Wallace, and D. Cowley, "Tests of a Precision Tiltmeter System for Measuring Telescope Position," *Proceedings of the SPIE*, vol. 3351, 1998.
- [37] M. Cullum and J. Spyromilio, "Thermal and Wind Control of the VLT," *Proceedings of the SPIE, Telescope Structures, Enclosures, Controls, Assembly/Integration/Validation, and Commissioning*, vol. 4004, 2000.
- [38] W. Gawronski, F. Baher, and O. Quintero: "Azimuth Track Level Compensation to Reduce Blind Pointing Errors of the Deep Space Network Antennas," *IEEE Antennas and Propagation Magazine*, vol. 42, pp. 28–38, 2000; also see tmo.jpl.nasa.gov/tmo/progress_report/42-139/139D.pdf
- [39] A. Greve, M. Dan, and J. Penalver, "Thermal Behavior of Millimeter Wavelength Radio Telescopes," *IEEE Transactions on Antennas and Propagation*, vol. 40, no. 11, pp. 1375–1388, 1992.

- [40] A. Greve and G. MacLeod, "Thermal Model Calculations of Enclosures for Millimeter Wavelength Radio Telescopes," *Radio Science*, vol. 36, no. 5, 2001.
- [41] W. Gawronski and B. Parvin, "Radiotelescope Low Rate Tracking Using Dither," *AIAA Journal of Guidance, Control, and Dynamics*, vol. 21, pp. 1111–1128, 1998.
- [42] C. H. Rivetta and S. Hansen, "Friction Model of the 2.5 mts SDSS Telescope," *Proceedings of the SPIE*, vol. 3351, 1998.
- [43] A. Ramasubramanian and L. R. Ray, "Adaptive Friction Compensation Using Extended Kalman-Bucy Filter Friction Estimation: A Comparative Study," *Proceedings of the American Control Conference*, Chicago, Illinois, 2000.
- [44] J. Moreno, R. Kelly, and R. Campa, "On Velocity Control Using Friction Compensation," *Proceedings of the 41st Conference on Decision and Control*, Las Vegas, Nevada, 2002.
- [45] M. Feemster, P. Vedagarbha, D. M. Dawson, and D. Haste, "Adaptive Control Techniques for Friction Compensation," *Proceedings of the American Control Conference*, Philadelphia, Pennsylvania, 1998.
- [46] M. Nordin and P. O. Gutman, "Controlling Mechanical Systems with Backlash—A Survey," *Automatica*, vol. 38, pp. 1633–1649, 2002.
- [47] R. Dhaouadi, K. Kubo, and M. Tobise, "Analysis and Compensation of Speed Drive System with Torsional Loads," *IEEE Transactions on Industry Applications*, vol. 30, no. 3, pp. 760–766, 1994.
- [48] M. T. Mata-Jimenez, B. Brogliato, and A. Goswami, "On the Control of Mechanical Systems with Dynamics Backlash," *Proceedings of the 36th Conference on Decision and Control*, San Diego, California, 1997.
- [49] B. Friedland, "Feedback Control of Systems with Parasitic Effects," *Proceedings of the American Control Conference*, Albuquerque, New Mexico, 1997.
- [50] J. L. Stein and C.-H. Wang, "Estimation of Gear Backlash: Theory and Simulation," *Journal of Dynamic Systems, Measurement, and Control*, vol. 120, 1998.
- [51] N. Sarkar, R. E. Ellis, and T. N. Moore, "Backlash Detection in Geared Mechanisms: Modeling, Simulation, and Experimentation," *Mechanical Systems and Signal Processing*, vol. 11, no. 3, pp. 391–408, 1997.
- [52] A. A. Stark, R. A. Chamberlin, J. G. Ingalls, J. Cheng, and G. Wright, "Optical and Mechanical Design of the Antarctic Submillimeter Telescope and Remote Observatory," *Rev. Sci. Instrum.*, vol. 68, pp. 2200–2213, 1997.
- [53] W. Gawronski, J. J. Brandt, H. G. Ahlstrom, Jr., and E. Maneri, "Torque Bias Profile for Improved Tracking of the Deep Space Network Antennas," *IEEE Antennas and Propagation Magazine*, vol. 42, pp. 35–45, December 2000; also see tmo.jpl.nasa.gov/tmo/progress_report/42-139/139F.pdf
- [54] W. Gawronski and E. Craparo, "Antenna Scanning Techniques for Estimation of Spacecraft Position," *IEEE Antennas and Propagation Magazine*, vol. 44, no. 6, pp. 38–45, December 2002; also see ipnpr.jpl.nasa.gov/tmo/progress.report/42-147/147B.pdf
- [55] N. Levanon, "Upgrading Conical Scan with Off-Boresight Measurements," *IEEE Transactions on Aerospace and Electronic Systems*, vol. 33, no. 4, pp. 1350–1357, 1997.

- [56] M. A. Gudim, W. Gawronski, W. J. Hurd, P. R. Brown, and D. M. Strain, "Design and Performance of the Monopulse Pointing System of the DSN 34-Meter Beam-Waveguide Antennas," *The Telecommunications and Mission Operations Progress Report 42-138, April-June 1999*, Jet Propulsion Laboratory, Pasadena, California, pp. 1-29, August 15, 1999, tmo.jpl.nasa.gov/tmo/progress_report/42-138/138H.pdf
- [57] W. Gawronski and M. A. Gudim, "Design and Performance of the Monopulse Control System," *IEEE Antennas and Propagation Magazine*, vol. 41, pp. 40-50, 1999; also see tmo.jpl.nasa.gov/tmo/progress_report/42-137/137A.pdf
- [58] <http://ipnpr.jpl.nasa.gov/>
- [59] deepspace.jpl.nasa.gov/dsn/
- [60] www.lmtgtm.org/
- [61] www.alma.nrao.edu/info
- [62] tmt.ucolick.org/
- [63] www.mmto.org/